

PAPER • OPEN ACCESS

A direct laser-synthesized magnetic metamaterial for low-frequency wideband passive microwave absorption


To cite this article: Yihe Huang *et al* 2023 *Int. J. Extrem. Manuf.* **5** 035503

View the [article online](#) for updates and enhancements.

You may also like

- [High thermal conductivity of hexagonal boron nitride laminates](#)
Jin-Cheng Zheng, Liang Zhang, A V Kretinin *et al.*
- [Breaking of equatorial symmetry in a rotating system: A spiralling intermittency mechanism](#)
J. M. Brooke
- [Operation of aerial inspections vehicles in HVDC environments Part B: Evaluation and mitigation of magnetic field impact](#)
M Heggo, A Mohammed, J Melecio *et al.*

A direct laser-synthesized magnetic metamaterial for low-frequency wideband passive microwave absorption

Yihe Huang^{1,9,10} , Yize Li^{2,10}, Kewen Pan^{3,10}, Yixian Fang², Kai Chio Chan^{4,5}, Xiaoyu Xiao², Chao Wei⁹, Kostya S Novoselov^{4,6,7,8}, John Gallop³, Ling Hao³, Zhu Liu⁹, Zhirun Hu^{2,4,*} and Lin Li^{1,9,*}

¹ Laser Processing Research Centre, Department of Mechanical, Aerospace and Civil Engineering, The University of Manchester, Oxford Road, M13 9PL Manchester, United Kingdom

² Department of Electrical and Electronics Engineering, The University of Manchester, Oxford Road, M13 9PL Manchester, United Kingdom

³ National Physical Laboratory, London, United Kingdom

⁴ National Graphene Institute, The University of Manchester, Oxford Road, M13 9PL Manchester, United Kingdom

⁵ Department of Materials, The University of Manchester, Oxford Road, M13 9PL Manchester, United Kingdom

⁶ Department of Physics and Astronomy, The University of Manchester, Oxford Road, M13 9PL Manchester, United Kingdom

⁷ Institute for Functional Intelligent Materials, National University of Singapore, 117544 Singapore, Singapore

⁸ Chongqing 2D Materials Institute, Liangjiang New Area, Chongqing 400714, People's Republic of China

⁹ Ningbo Institute of Materials Technology and Engineering, Chinese Academy of Sciences, Ningbo 315201, People's Republic of China

E-mail: lin.li@manchester.ac.uk and zhirun.hu@manchester.ac.uk

Received 14 February 2023, revised 28 March 2023

Accepted for publication 20 April 2023

Published 4 July 2023



CrossMark

Abstract

Microwave absorption in radar stealth technology is faced with challenges in terms of its effectiveness in low-frequency regions. Herein, we report a new laser-based method for producing an ultrawideband metamaterial-based microwave absorber with a highly uniform sheet resistance and negative magnetic permeability at resonant frequencies, which results in a wide bandwidth in the L- to S-band. Control of the electrical sheet resistance uniformity has been achieved with less than 5% deviation at $400 \Omega \text{ sq}^{-1}$ and 6% deviation at $120 \Omega \text{ sq}^{-1}$, resulting in a microwave absorption coefficient between 97.2% and 97.7% within a 1.56–18.3 GHz bandwidth for incident angles of 0° – 40° , and there is no need for providing energy or an electrical power source during the operation. Porous N- and S-doped turbostratic graphene 2D patterns with embedded magnetic nanoparticles were produced simultaneously on a polyethylene terephthalate substrate via laser direct writing. The proposed low-frequency,

¹⁰ Those authors have equal contributions to this work.

* Authors to whom any correspondence should be addressed.



Original content from this work may be used under the terms of the [Creative Commons Attribution 4.0 licence](https://creativecommons.org/licenses/by/4.0/). Any further distribution of this work must maintain attribution to the author(s) and the title of the work, journal citation and DOI.

wideband, wide-incident-angle, and high-electromagnetic-absorption microwave absorber can potentially be used in aviation, electromagnetic interference (EMI) suppression, and 5G applications.

Keywords: laser direct writing, degrees of crystallization, Fe₃O₄ nanoparticles, wide bandwidth, low frequency

1. Introduction

Microwave absorbers are typically required for aircraft radar cross-section reduction. It is desirable to have a wide absorption bandwidth and a low-profile structure. These two requirements are often in conflict, particularly for frequencies lower than the X-band. Since the first experimental demonstration of metamaterial absorbers (MMAs) by Landy *et al* in 2008 [1], metamaterial-based absorbers have received increasing attention over the past decade owing to their low-profile advantage. In the early 2000s, the majority of traditional MMA designs relied on chemical etching [2] or computer numerical control machining [3] to meet the requirements for conformal production; however, the absorber performance was unsatisfactory. In the late 2000s, new MMA fabrication methods were introduced, such as ink-jet printing [4] and additive manufacturing [2]. Among the MMA printing techniques, conductive carbon-based printing has provided the best overall performance for MMAs [5]. Therefore, the majority of previous investigations over the past decade have been focused on inkjet printing technology for depositing carbon-based conductive inks owing to its high resolution at the microscale level and the high uniformity of the deposited layer thickness [6]. The sheet resistance tolerance of ink-jet printed carbon-based thin films (graphene <5% [7]; reduced graphene oxide (rGO) and carbon black <3% [8]; carbon nanotube <5% [9]) can be controlled well. However, to obtain the desired sheet resistance (especially a sheet resistance of less than 1000 ohm sq⁻¹), an inkjet printer must print hundreds of layers [10], which hinders its practical application. Spray printing and screen-printing technologies have been investigated as alternative methods owing to their excellent manufacturing efficiencies [11]. However, these macroscale printing methods have the disadvantages of complicated procedures, poor uniformity, and poor resolution. Ink preparation for the control of sheet resistance, magnetic permeability, and adhesion is a necessary further manufacturing step following material synthesis [12, 13]. The film thickness varied significantly between the pattern centre and edge, resulting in large variations in the sheet resistance. The sheet resistance variation of spray-printed and screen-printed graphene laminates is typically an order higher than that of inkjet printing (screen printing: 16%–33% [14] and 45% [12]; spray printing: 36% [15] and 40% [16]). To satisfy the more precise sheet-resistance variation requirements for modern MMAs, it is desirable to find a new fabrication method that combines more accurate sheet-resistance control with high productivity. Nevertheless, owing to the nature of electromagnetic waves and the electric boundary

conditions [17], effective absorption of lower-frequency electromagnetic waves requires a thicker absorber. The trade-off between the absorber thickness and low operating frequency is a challenging issue to address when designing broadband absorbers. It is necessary to combine the three aspects of the absorbing material, absorber structure design, and fabrication method [18] for producing a practical metamaterial microwave absorber.

Laser fabrication of MMAs including laser surface treatment [19, 20], laser etching [21, 22], laser ‘thick film’ printing [22], and laser graphitisation [23] was recently attempted. Laser surface treatments and etching technologies have been used to successfully fabricate conformal MMA structures. However, the microwave performance was not ideal owing to the limitations of the MMA material. The ‘thick film’ mould method involves the use of a laser to create a reversed pattern on a metal film, and conductive inks are then added for printing. These laser-based MMA fabrication methods focus on achieving a higher resolution of the MMA pattern rather than on improving the sheet resistance uniformity, which is key for broad-band MMA.

In our previous study, the laser direct synthesis and writing of functionalised graphene were investigated. Controlling the graphitisation of an organic precursor with an ultraviolet (UV) laser opens up a new possibility for controlling the electrical properties, which could significantly impact the MMA performance [24]. Compared with the aforementioned techniques for MMA fabrication, laser direct writing (LDW) has the potential to print nanocomposite materials with higher sheet resistance uniformity [25–28]. The capability of *in situ* nanomaterial generation during LDW is also advantageous [29, 30].

In this study, a specifically designed conductive pattern with well-controlled electrical characteristics was manufactured on a flexible polyethylene terephthalate (PET) substrate using UV laser processing. A laser-induced doped graphene (LIDG) pattern with induced magnetic nanoparticles forms a metasurface structure (with negative magnetic permeability). The sheet resistance of LIDG could be precisely controlled by varying the degree of crystallisation. Magnetic ferric oxide nanoparticles were simultaneously generated and embedded in graphene to increase the absorption bandwidth of the MMAs. This structure has demonstrated an ultra-wideband with very-low-frequency microwave absorption. This technique achieved patterning, control of sheet resistance and its uniformity, and synthesis of magnetic nanoparticles in a single step, thus demonstrating a significant advantage in terms of manufacturing efficiency.

2. Experimental section

2.1. Formulation of an organic donor ink

The precursor organic ink was composed of polybenzimidazole (PBI) and dimethyl sulfoxide (DMSO) at a 10 wt% PBI concentration. It was prepared by refluxing for 1 h at 140 °C. To generate embedded ferro ferric oxide into the LIDG, iron (II) acetate was introduced into the organic ink at 1 wt% concentration and uniformly dissolved in the ink with an additional half hour of reflux at 140 °C, which is lower than the thermal decomposition temperature of iron (II) acetate of 150 °C [31].

2.2. Coating preparation

The ink was coated on PET using a doctor blade (supplied by TOB Co. Ltd) at a running speed of 10 mm s⁻¹ and a 100 μm space (wet coating thickness). This laser technique could be applied to a wide range of substrates. Polymer was selected because PET does not influence the measurement results of the microwave absorption because its permittivity is equal to that of air. The solution was then dried for 30 min in a vacuum oven at 80 °C. The coating thickness was 12–14 μm after drying.

2.3. Laser synthesis and direct writing procedure

The LDW process was performed under ambient conditions, using an Edgewave picosecond laser with a pulse width of 10 ps and a laser fluence of 5.74–10.12 mJ cm⁻², operating at 355 nm laser wavelength, at a pulse repetition rate of 4047.4 kHz, and a scanning speed of 100 mm s⁻¹ using a galvo x-y scanner. The diameter of the focused beam spot on the target surface was 40 μm, while the hatch distance for the laser scanning was 20 μm.

2.4. Material characterisation

Raman spectroscopy was conducted on the laser-processed samples using a single excitation wavelength of 514 nm. Field-emission gun scanning electron microscopy (Zeiss Merlin scanning electron microscope with Gemin II) and scanning transmission electron microscopy (Talos F200X) were performed at 200 keV. X-ray photon-spectrometry (XPS) and x-ray diffraction were used to investigate the atomic structure and surface morphology of the resulting materials. XPS analysis was performed using Kratos Axis Ultra facility equipped with a monochromatic Al-K x-ray source. High-resolution core-level spectra were acquired using a hemispherical energy analyser positioned along the surface norm, with a pass energy of 20 eV. The spectra were calibrated by assigning a binding energy of 689 eV to the CF₂ component at the 1 s core level. XPS core-level profiles were fitted with CasaXPS software using a Gaussian–Lorentzian line shape.

A contact probe station (Jandel, RM3000) and semiconductor characterisation system (Keithley, 4200C) were used to measure the sheet resistance. The carrier mobility was measured using a precision DC Van der Pauw Hall measurement. A static magnetic field was generated using a GMW Magnet

3473, and the electric signal was collected using a Keithley precision source meter 2400 series. The system was controlled using a custom LabVIEW program. During measurement, the DC magnet was set to 0.4 T and the measurement current was 10 μA.

2.5. Meta-structure design and microwave absorption measurement procedure

The proposed ultra-wideband microwave absorber was designed and simulated using CST Microwave Studio. The absorbers were mechanically assembled in the following order: silica gel, circular metamaterial layer, silica gel, square metamaterial layer, and copper ground. Two horn antennas (Aaronia AG, PowerLOG 70180) from 700 MHz to 18 GHz were connected to a calibrated VNA (FieldFox Microwave Analyser N9918A, Keysight) as the transmitter and receiver to measure the microwave absorption characteristics. The entire measurement process was carried out in an anechoic chamber.

3. Results and discussion

3.1. Meta-surface simulation and design

Square- and circular-shaped metamaterial elements were selected owing to their straightforward geometry and sufficient impedance matching to facilitate the design of the absorber. The metamaterial elements with a solid layout (square and circular) were capacitive. Changes in the shape result in different equivalent resistances and capacitances. The equivalent inductance or capacitance change is very small for the different shapes; however, this does affect matching conditions with free space. The simulated electromagnetic performance of the design was obtained using CST Microwave Studio [32]. The simulated surface power loss density of the three absorption peaks at 2.9 GHz, 7.5 GHz, and 17.3 GHz are presented in figure 1. For a lower absorption frequency (approximately 2.9 GHz), the surface power loss was mainly localised between the square layers (120 Ω sq⁻¹). As the frequency increased to 7.5 GHz, the localised surface power loss moved towards the top circular layer (400 Ω sq⁻¹). In the case of the higher frequency bands, absorption occurs owing to the combined effect of the surface currents on both layers.

The structure of the proposed MMA was designed to achieve ultrawideband microwave absorption, as shown in figure 2(a), and consists of a 12 × 12 elementary unit cell array. Its dimensions were 240 mm × 240 mm × 15.5 mm. The squares and circles were subjected to laser irradiation and became impedance surfaces. The unirradiated material and ink do not affect the microwave absorption; thus, they do not need to be removed. The basic unit comprised two impedance surfaces, three dielectric substrate layers, and a ground plane. The top wide-angle impedance matching (WAIM) [33] and middle layers (Sub.1 in figure 2(a)) were both fabricated from silicone (Polymax, SILONA translucent Silicone Sheet GP) with a 4 mm thickness, a 2.9 dielectric constant, and a loss tangent of 0.1. The bottom layer (Sub.2 in figure 2(a)) consisted of 6 mm

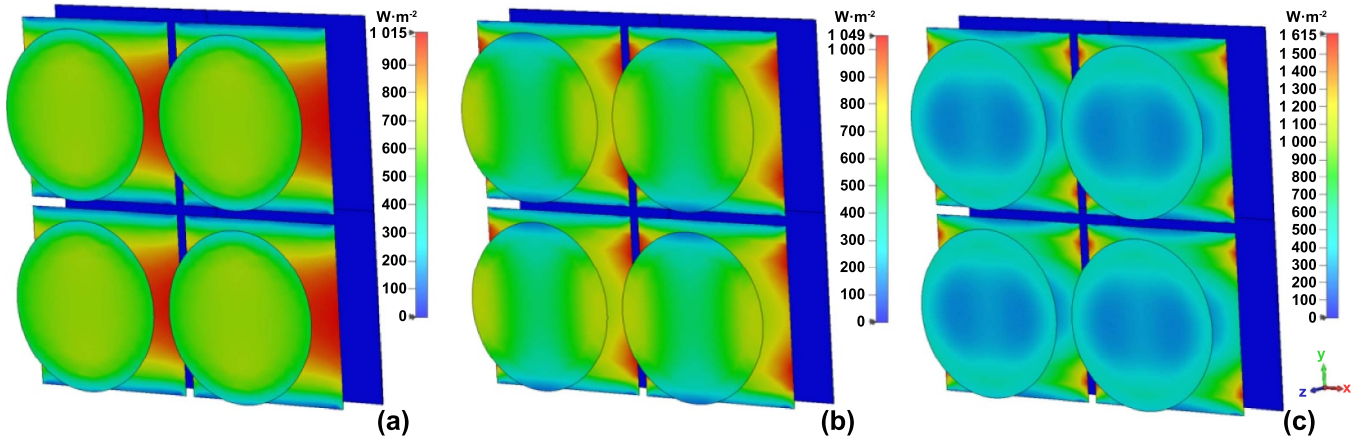


Figure 1. Simulated surface power loss density of the absorber at (a) 2.9 GHz, (b) 7.5 GHz, and (c) 17.3 GHz.

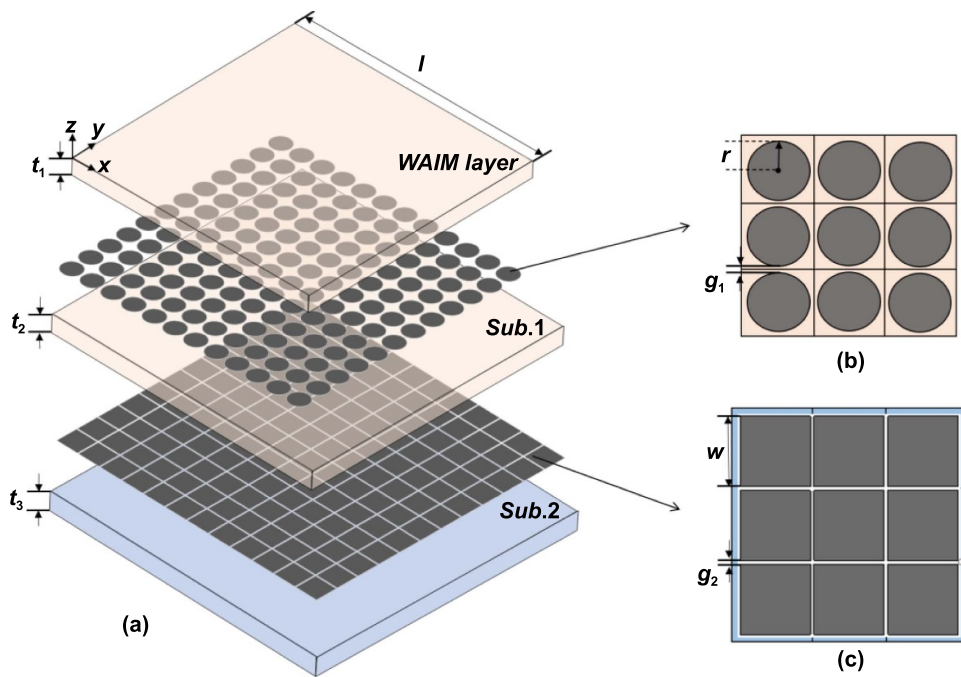


Figure 2. Proposed multilayer metamaterial absorber (MMA) (a) explosive view: $t_1 = t_2 = 4$ mm, and $t_3 = 5$ mm. (b) LIDG circular pattern: $r = 9$ mm, and $g_1 = 2$ mm. (c) LIDG surface model having a square pattern: $w = 19$ mm, and $g_2 = 1$ mm.

polyurethane foam sheets with a 1.05 dielectric constant and a loss tangent of 0.02. Circular and square LIDG patterns of different sheet resistances ($400 \Omega \text{ sq}^{-1}$ and $120 \Omega \text{ sq}^{-1}$, respectively) were printed on PET. A pure copper sheet of the same size was placed at the back of the absorber as the ground plane. The metamaterial unit cells were set by applying periodic conditions across the unit cells of the structure during the simulation. The multilayer structures were periodically arranged on the substrates. The reflection coefficient depends on the local characteristics of the multilayer structures and the interactions between neighbouring cells. The simulated absorption bandwidth of the proposed absorber was approximately 162%.

3.2. One-step laser synthesis LIDG embedded with Fe_3O_4

Figure 3(a) illustrates the LDW procedure used for the PET. The silver-black laser-irradiated tracks were the result of laser-induced graphitisation. The morphology of the laser-graphitised PBI exhibited different levels of pores, as shown in figure 3(b), while the laser-graphitised in the presence of Fe_3O_4 nanoparticles showed significantly fewer nanopores (figure 3(c)). The thickness of the graphitised layers was approximately $10 \mu\text{m}$, which is less than the original thickness of $12\text{--}14 \mu\text{m}$ owing to the self-release of CO_x and NO_x gases, which prevented the oxidation of the graphitised layers dur-

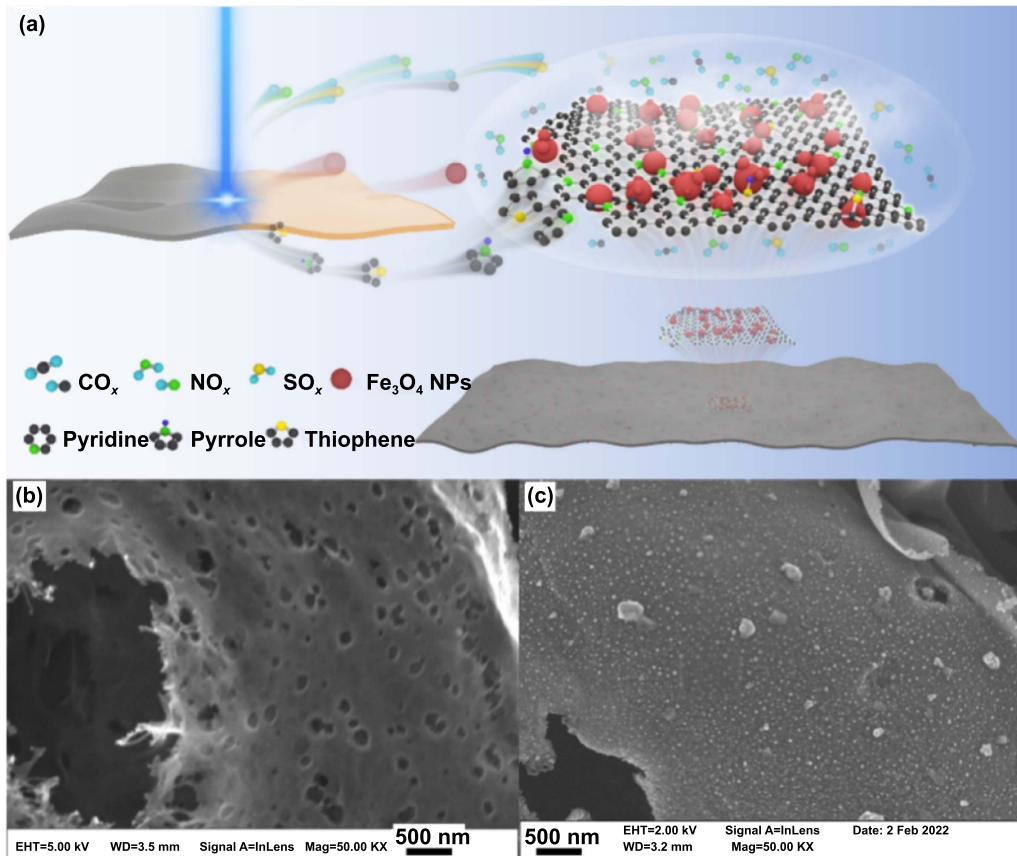


Figure 3. Schematic (a) of LIDG fabrication and surface morphology difference between LIDG without (b) and with (c) nanoparticles embedded.

ing the laser process. It is worth noting that a layer of PBI remained beneath the graphitised layer, which was adhered to the PET substrate. Therefore, it is important to ensure that the graphitisation depth is less than the total thickness of the coating.

Compared with the C–S bond energy (2.8 eV) in the DMSO and the C–N bond energy (3.14 eV) in PBI, the high 3.49 eV photon energy from the 355 nm wavelength laser resulted in both photochemical and photothermal reactions when interacting with the coated material. The laser processing decomposed the PBI and DMSO at low laser powers into free radical benzene rings as a carbon-source material; free radical dopant elements such as thiophene, pyrrolic, and pyridine; and protective gases, including NO, NO₂, CO, CO₂ and SO₂. From the XPS spectra presented in figure 4, 91.52% sp² (284.5 eV) originated from the crystallite LIDG. The N and S doping in the LIDG contributes to p electrons of the π system, which can promote the electrical conductivity of LIDG. The S(2p_{3/2}, 2p_{1/2}) covalent bond of thiophene at 163.5 eV and 164.7 eV is observed in the graphene structure owing to the spin-orbit couplings. This originates from the photochemical decomposition of the DMSO during graphene synthesis [24]. The N covalent bonds of pyrrolic and pyridinic at 400 eV and 398 eV, respectively, in the graphene structure were different from those in the absence of iron acetate. The concentration ratio of pyrrolic N and pyridinic N was 47:53,

which is slightly lower than the concentrate ratio (39.1:29.7) without iron acetate. A greater amount of pyridinic N resulted in fewer edge defects and more abundant mesopores, the majority of which were occupied by nano-Fe₃O₄ (figure 3(c)). Therefore, the addition of iron II acetate had a thermal effect on the pyridinic N generation and inhibited oxidation, in contrast to the case of the LIDG fabricated using an infrared laser, which would be dominated by the thermal effect [24].

Owing to the multiple reactions, iron (II) acetate was decomposed by laser irradiation in air. The element distribution mapping of the nanoparticles, as shown in figures 5(a₁), (a₂) and (a₃) demonstrates the generation of magnetic particles of approximately 10 nm in size. The decomposition temperature of iron acetate in air exceeds 290 °C. With an increase in the temperature, magnetite Fe₃O₄ was initially generated and was subsequently oxidised into haematite with a longer treatment or higher temperature. In figure 5(b₁), the Fe 2p peak of Fe₃O₄ was deconvoluted into Fe²⁺ and Fe³⁺ peaks. The peak positions of Fe 2p_{3/2} and Fe 2p_{1/2} were 710 eV and 723.8 eV, respectively. The binding energy of the O 1s peak for Fe₃O₄ is commonly at 530 eV, as illustrated in figure 5(b₂), and that for Fe₂O₃ was at approximately 527 eV [34]. Moreover, the high reaction kinetics, due to the longer reaction time and higher temperature, caused an increase in the size of the nanoparticles [35]. The fast laser processing speed with

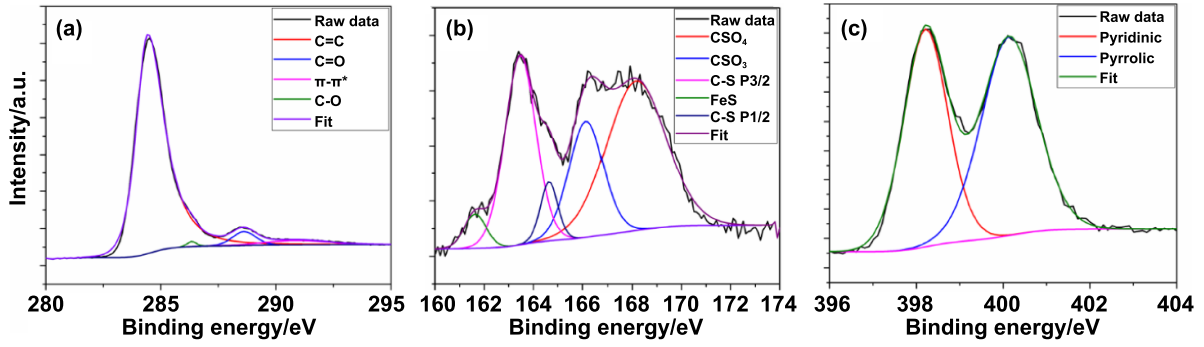


Figure 4. XPS spectra of the LIDG with nano-Fe₃O₄ embedded: (a) carbon, (b) sulphur, and (c) nitrogen.

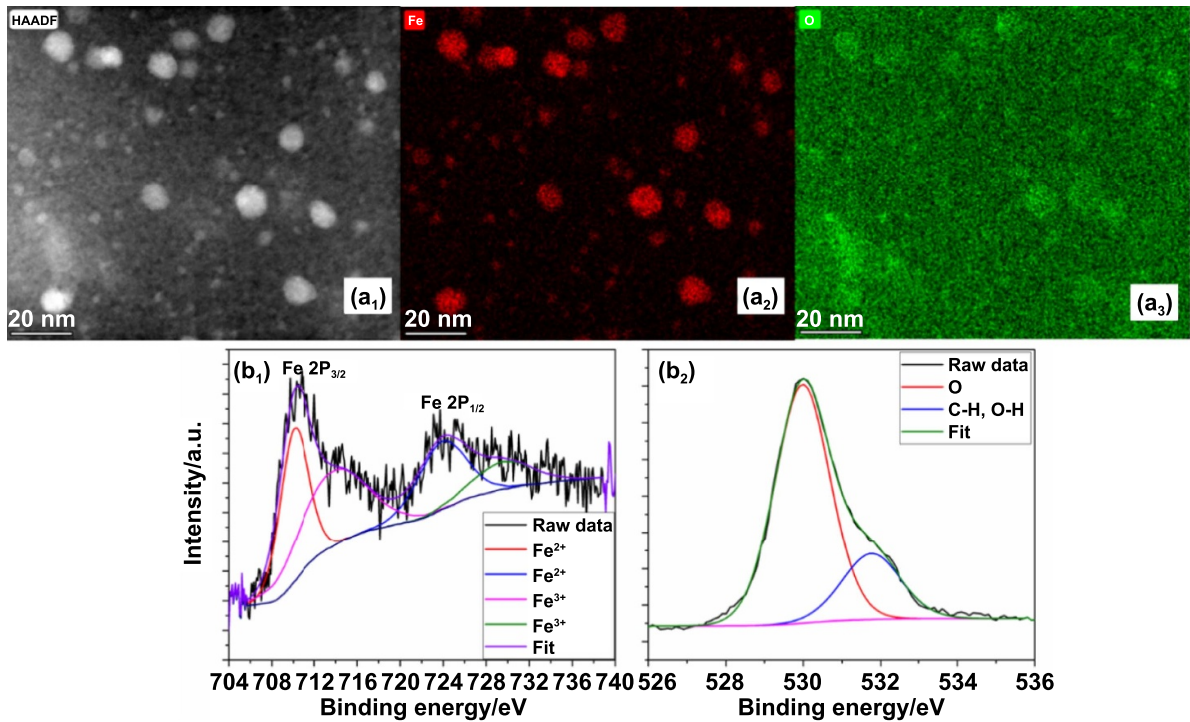


Figure 5. STEM energy dispersive x-ray spectroscopy image (scale bar: 20 nm): (a₁) morphology, (a₂) Fe, (a₃) O; XPS spectra for nano-Fe₃O₄ particles in LIDG: (b₁) Fe; and (b₂) O.

controlled thermal effects realized by selecting an appropriate laser power and repetition rate can generate nanoparticles of a specific size from a liquid precursor and effectively minimise overtreatment to avoid thermal damage to both the coating and substrate.

3.3. Sheet resistance control and Raman spectra

Precise control of laser graphitisation is important for tuning the electrical properties of LIDG. The laser fluence on the PBI pattern was gradually increased from 5.74 mJ cm⁻² to 10.12 mJ cm⁻² to study the relationship between the laser-induced graphitisation and the electrical properties of the material after the laser processing. As shown in figure 6(b), the increasing ratio of the Raman spectra *D* peak (1350 cm⁻¹) over the *G* peak from 0.92 to 1.34 during the crystallisation

stage provides evidence that the degree of carbon crystallisation gradually increases [36]. The sp² crystal length (*L*_α) can be expressed as [37]

$$\frac{I(D)}{I(G)} = C'(\lambda)L_{\alpha}^2 \quad (1)$$

where *C'* is a constant related to the wavelength (λ) of the Raman spectralaser. The decreased ratio of the Raman spectrum *D* peak (1350 cm⁻¹) over the *G* peak from 1.34 to 1.29 was in the defect reducing stage. At this stage, *L*_α is expressed as

$$L_{\alpha} = 2.4 \times 10^{-4} \lambda^4 \frac{I(G)}{I(D)}. \quad (2)$$

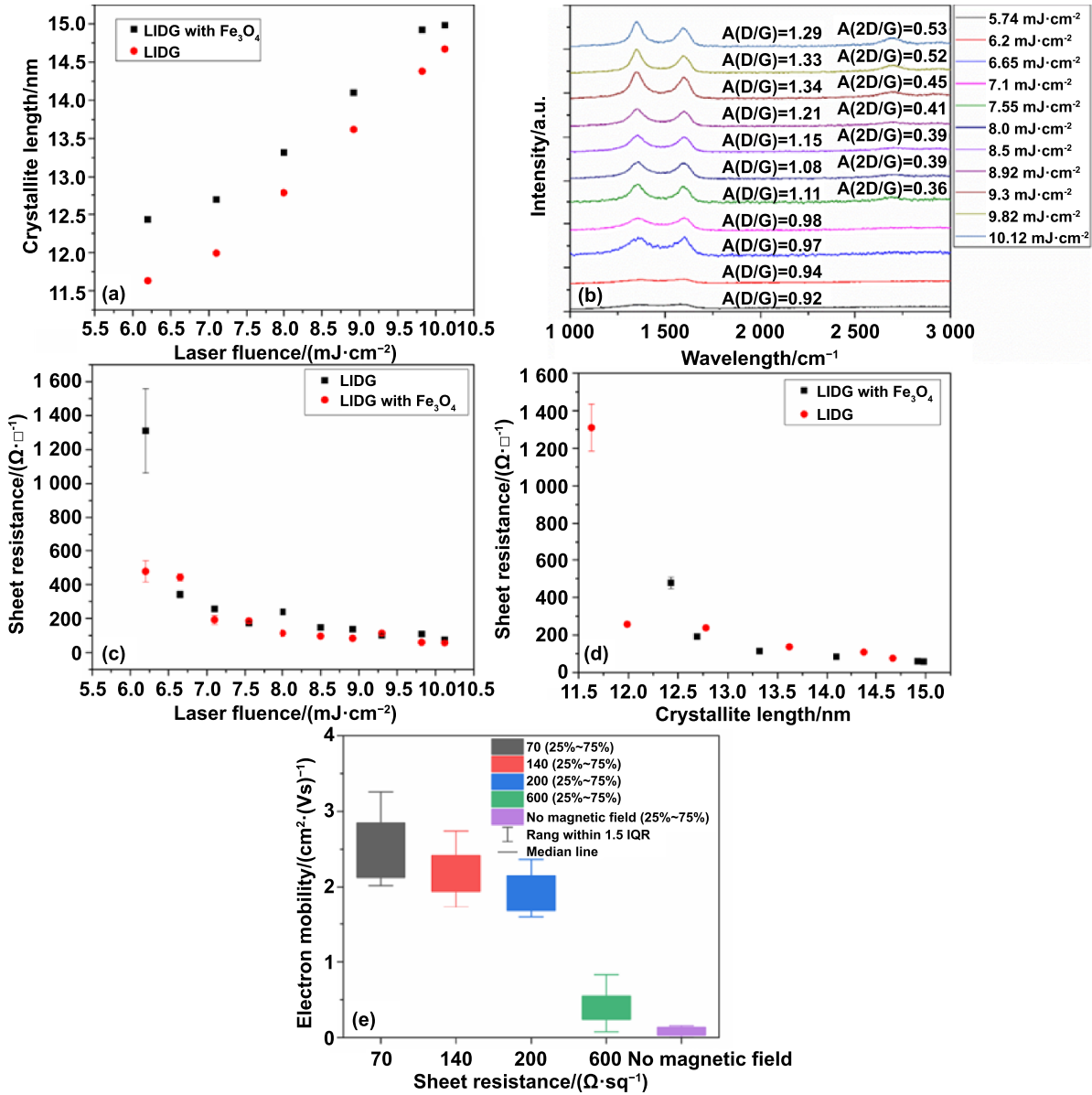


Figure 6. Alternative crystallite length (a) and Raman Spectra (b) with various laser fluences, alternative laser fluence (c), crystallite length (d), and electron mobility (e) with various sheet resistances from LIDG with/without Fe₃O₄.

In figure 6(a) the crystal length of LIDG with/without nano-Fe₃O₄ was respectively enhanced from 12.4 to 15 nm and from 11.6 nm to 14.6 nm, owing to the sp² C–C bond restoration induced by the gradually increased thermal heating [38]. The thermal energy from iron oxidation resulted in larger crystals than those of pure LIDG. The increase in the laser fluence from 6.2 to 10.12 mJ cm⁻² resulted in an increase in the crystal length, which resulted in the increase of the sheet resistance from 75 to 1310 Ω sq⁻¹. Enhanced graphene crystallisation from the growth of the crystal length can effectively promote electron mobility, as shown in figure 6(e). The volume of the sp² bond structure-controlled electron carrier concentration and electron mobility are inversely correlated with the sheet resistance with a constant sample thickness of approximately 3 μm [39, 40]. Thus, the sheet resistances of LIDG with and without nano-Fe₃O₄ were reciprocally related

to the length of the crystal. Under the same laser conditions, the sheet resistance of LIDG with nano-Fe₃O₄ ranged from 57 to 480 Ω sq⁻¹. The initial 0.8 nm difference between 11.6 nm and 12.4 nm in figure 6(a), due to thermal heating of 3 wt% iron(II) acetate, can effectively reduce the sheet resistance from 1310 Ω sq⁻¹ to 480 Ω sq⁻¹ with a standard deviation from 20% to less than 5%, as shown in figure 6(d). With an increase in the laser fluence, the difference in the crystal length and sheet resistance between the LIDG with and without nano-Fe₃O₄ gradually vanished because complete crystallisation occurred, and the excess energy could only damage the sp² structure. The controlled deviation ratio of the sheet resistance was between 4% and 6%, when the laser fluence was between 5.74 and 10.12 mJ cm⁻², as shown in figure 6(c). It is worth noting that the uniformity of the sheet resistance was determined by the thickness and uniformity of

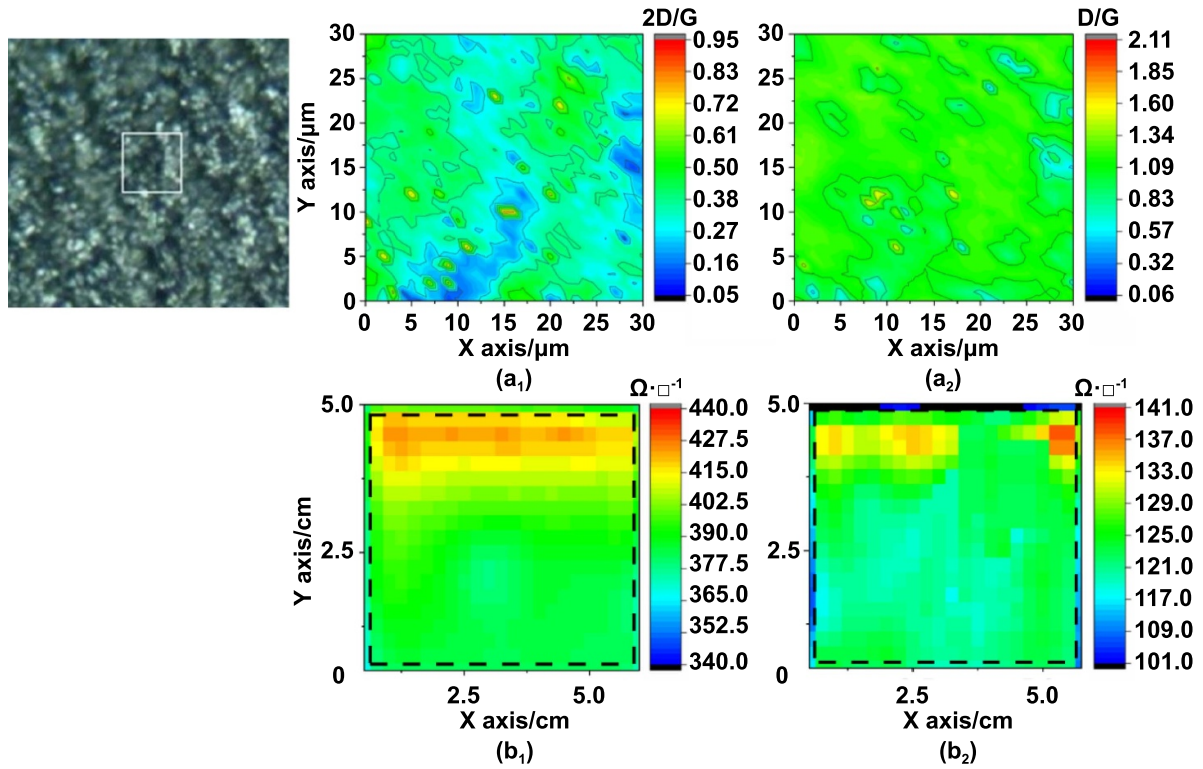


Figure 7. Raman spectra mapping: (a₁) 2D/G and (a₂) D/G, and sheet resistance mapping: (b₁) $400 \Omega \text{ sq}^{-1}$ and (b₂) $120 \Omega \text{ sq}^{-1}$.

the graphitised layers, rather than the uniformity of the original coating.

The increasing ratios of the Raman spectra 2D peak (2700 cm^{-1}) over the G peak, in the range of 0.36–0.53, provide evidence for the formation of graphene (with less than five layers) and the reduction of amorphous carbon. The increased intensity and symmetric broadening of the 2D peak, as shown in figure 6(b), was owing to the formation of a turbostratic graphene structure, which was due to the *in-situ* doping and the flow of the protection gas [41].

The 2D Raman spectrum mapping of LIDG embedded with nano- Fe_3O_4 , as shown in figures 7(a₁) and (a₂), demonstrates the uniformity of the resulting graphene and is indicated by the colour intensity as the ratios of $I(2D)/I(G)$ and $I(D)/I(G)$. The mean values of the $I(2D)/I(G)$ ratio were approximately 0.4. The areas wherein the laser was applied more than once exhibited a relatively higher value of $I(2D)/I(G)$, indicating that laser annealing improved the quality of graphene.

The overlapping of the laser-scanned tracks had no impact on the uniformity of the crystallisation, as demonstrated by the mean values of $I(D)/I(G)$. The sheet resistance mappings of LIDG embedded with Fe_3O_4 and irradiated at a laser fluence of 6.65 mJ cm^{-2} and 9.82 mJ cm^{-2} are presented in figures 7(b₁) and (b₂), respectively. Both show a high degree of uniformity with less than a 5% and 6% deviation for the designed LIDG with $400 \Omega \text{ sq}^{-1}$ and $120 \Omega \text{ sq}^{-1}$, as shown in figures 7(b₁) and (b₂), respectively.

3.4. Comparisons between simulation and measurement results for microwave absorption

Figures 8(a) and (b) present photographs of the two LIDG pattern layers. The MMA was mechanically assembled using polymeric fixtures, as shown in figure 2(a). The distance between the MMA and antennas is 1.8 m in figure 8(c).

3.4.1. Effects of pure LIDG on absorption. Figures 9(a) and (c) present a comparison between the simulated and measured absorptions at normal incidence for the transverse-electric (TE) and transverse-magnetic (TM) polarisations. As shown in figure 9(a), the measured absolute bandwidth of the absorber ranged from 1.85 GHz to 18.2 GHz, and the measured fractional absorption bandwidth was approximately 163% in the TE mode under normal incidence. Similarly, for normal incidence under the TM mode, the MMA exhibits ultra-wide fractional absorption bandwidth of approximately 169% from 1.56 GHz to 18.3 GHz. In addition, for both the TE and TM modes, the proposed MMA had an impressive average absorption coefficient within its operating bandwidths of 97.2% and 97.7%, respectively. Furthermore, the absorption bandwidth and absorption coefficient of the proposed MMA exhibited minimal variations across both the TE and TM modes owing to its symmetrical shape. The experimental observations agree with the numerical results; this can be attributed to the utilisation of LIDG technology, which ensures accurate control of the sheet resistance within a 5% accuracy.

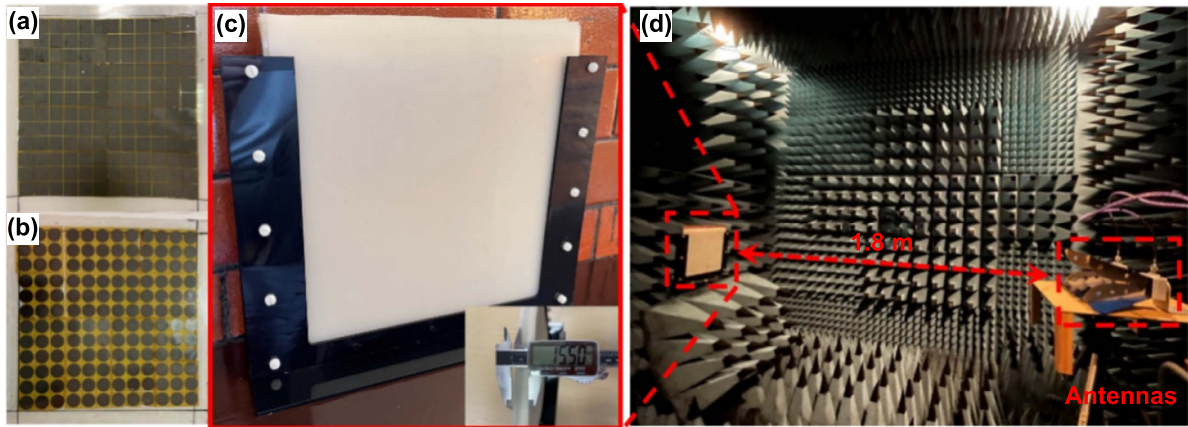


Figure 8. Microwave measurement setup: (a) LIDG square patterns. (b) LIDG circular patterns. (c) Photograph of the MMA and measured total thickness of 15.5 mm. (d) Absorption measurement setup in the anechoic chamber.

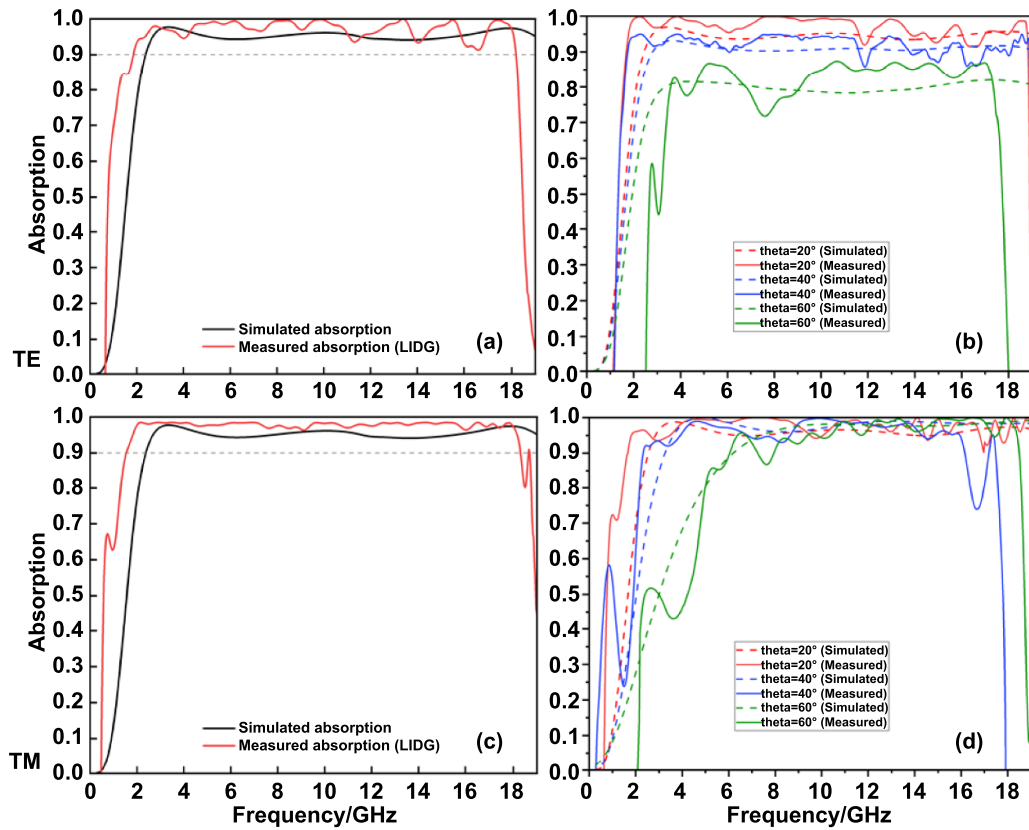


Figure 9. Comparison of simulation and measurement results of LIDG absorber: (a) TE mode under normal incidence. (b) TE mode under oblique incidences. (c) TM mode under normal incidence. (d) TM mode under oblique incidences.

To further analyse the performance of the absorber, the absorption of oblique incidences at 20°, 40° and 60° for the TE and TM polarisations was measured and compared with the corresponding simulation results in figures 9(b) and (d). When the incident angle is 20°, for both the TE and TM modes, the absorber can maintain a nearly identical fractional absorption bandwidth and the same absorption coefficient as that under normal incidence. When the incident angle was

increased to 40°, the absorber still had a wide fractional bandwidth of approximately 110% and 118% for the TE and TM modes, respectively, and provided over 93% absorption under both radiations. In the TE mode, when the incident angle was increased to 60°, the absorber lost its broadband characteristics, but it could still provide over 85% absorption within the majority of the frequency bands. Similarly, at an incident angle of 60° in the TM mode, the fractional bandwidth of

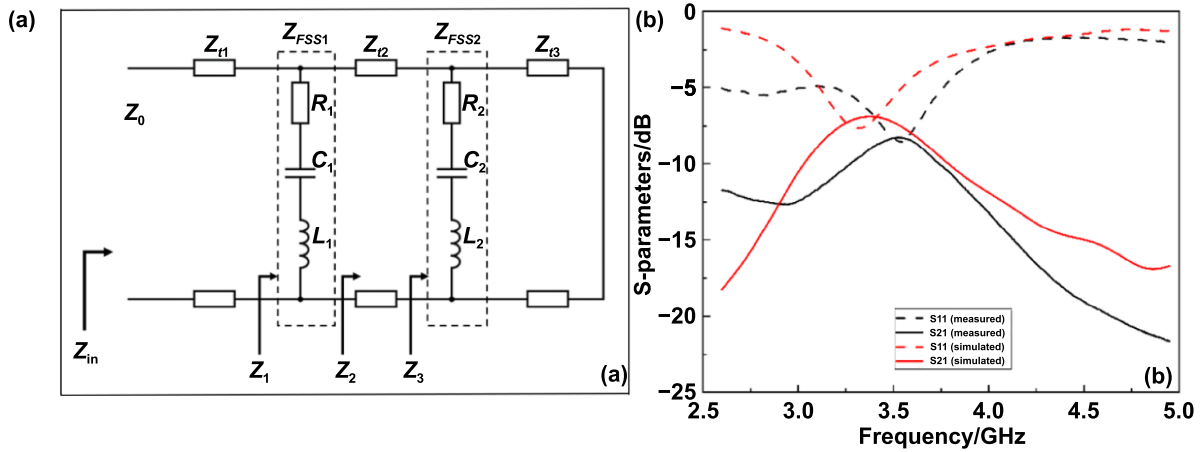


Figure 10. Qualitative analysis of the microwave absorber: (a) transmission line equivalent circuit model of the metamaterial absorber. (b) Measured and simulated S-parameters of ring resonator (RR) with Fe_3O_4 -embedded LIDG layer.

the absorber decreased to 75.3%, with an average absorption of approximately 95%. The measured results demonstrated an excellent absorption performance at oblique incidence angles.

3.4.2. Effects of embedded Fe_3O_4 nanoparticles on absorption. The electromagnetic resonance of a MMA is the key to achieving good absorption. Electromagnetic resonance causes disturbances that result in the attenuation of electromagnetic waves [42]. Therefore, impedance matching between the free space and the metamaterial structure is crucial. A transmission-line equivalent circuit model of the proposed absorber is presented in figure 10(a). The WAIM layer and dielectric substrate are modelled as transmission lines. According to the transmission line theory and the calculation method used in [43, 44] the input impedance can be represented as

$$Z_{\text{in}} = Z_{r1} \frac{z_1 + jz_{t1} \tan\left(\frac{2\pi f}{c} \sqrt{\epsilon_{rs}} Z_{r1}\right)}{z_{t1} + jz_1 \tan\left(\frac{2\pi f}{c} \sqrt{\epsilon_{rs}} Z_{r1}\right)} \quad (3)$$

$$Z_1 = Z_{\text{FSS1}} \parallel Z_{r2} \quad (4)$$

$$Z_2 = Z_{r2} \frac{z_3 + jz_{t2} \tan\left(\frac{2\pi f}{c} \sqrt{\epsilon_{rs}} Z_{r2}\right)}{z_{t2} + jz_3 \tan\left(\frac{2\pi f}{c} \sqrt{\epsilon_{rs}} Z_{r2}\right)} \quad (5)$$

$$Z_3 = Z_{\text{FSS2}} \parallel Z_{r3} \quad (6)$$

$$Z_{r3} = j \frac{z_0}{\epsilon_{rf}} \tan\left(\frac{2\pi f}{c} \sqrt{\epsilon_{rf}} Z_{r3}\right) \quad (7)$$

$$Z_{\text{FSS}_k} = R_k + j\omega L_k - \frac{j}{\omega C_k}, k = 1, 2 \quad (8)$$

where ' t_1 , t_2 , and t_3 ' are the thicknesses of the dielectric substrate and the WAIM layer. ϵ_{rs} and ϵ_{rf} are the relative permittivities of the silicone substrates, respectively. The free space impedance is represented by Z_{in} at 377Ω . To match the free space impedance, the lumped elements are derived and calculated as $R_1 = 620 \Omega$, $R_2 = 145 \Omega$, $C_1 = 0.075 \text{ pF}$, $C_2 = 0.4 \text{ pF}$, $L_1 = 1.15 \text{ nH}$, and $L_2 = 0.15 \text{ nH}$.

The relative permeability (μ_r) was tuned to enhance the impedance matching between the MMA and free space. A small amount of Fe_3O_4 was embedded into the LIDG using the LDW technique. As the majority of magnetic materials have a high relative permeability, the amount of Fe_3O_4 mixed in the conductive layer must be controlled precisely within an acceptable minimum range. To measure the magnetic permeability of Fe_3O_4 embedded in the LIDG thin film, a ring resonator (RR) with a coplanar waveguide (CPW) feed was fabricated and an Fe_3O_4 embedded LIDG layer ($400 \Omega \text{ sq}^{-1}$) was affixed at the centre of the resonator [12]. The complete model of the resonator with the LIDG was reproduced in CST. Figure 10(b) presents the simulated and measured S-parameters of the RR, where μ_r was continuously adjusted until similar trends were observed. The relative permeability (μ_r) of the LIDG embedded with Fe_3O_4 was approximately 3 with a tangent delta magnetic field of 0.1.

Figure 11 presents the measured absorptivity performance of the LIDG MMA with and without the embedded nano-magnetic Fe_3O_4 for various incident angles from 0° to 60° under TE and TM polarisations. As shown in figure 11(a), compared with the MMA without Fe_3O_4 , the Fe_3O_4 embedded MMA has a wider bandwidth from 1.46 GHz to 18.8 GHz, at approximately 171% in the TE mode under normal incidence. Owing to the symmetrical construction, the Fe_3O_4 embedded MMA in the TM mode with normal incidence also had a wide fractional bandwidth of approximately 173%, from 1.32 GHz to 17.9 GHz. The bandwidth of the MMA increased by approximately 4%–8% with Fe_3O_4 . It can be observed that

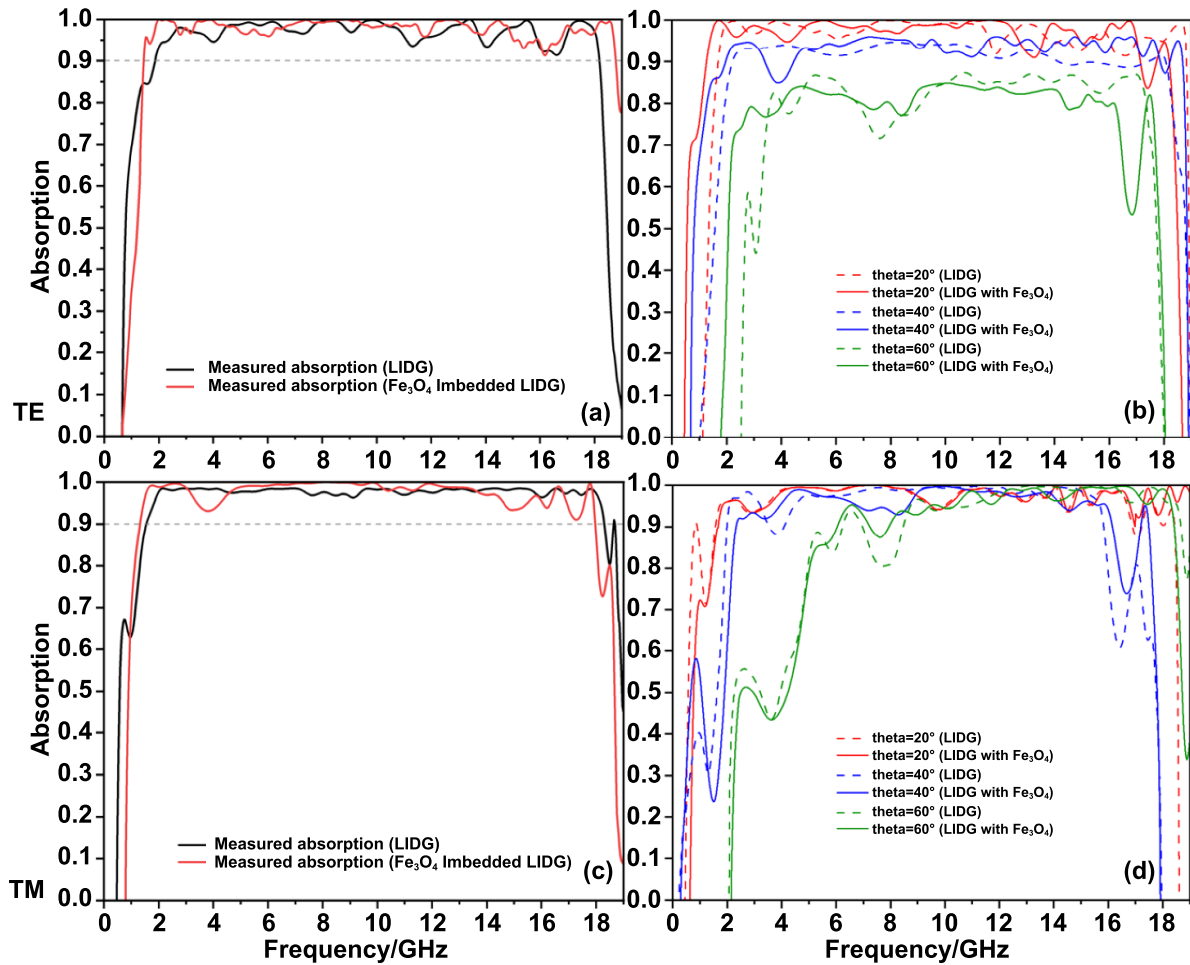


Figure 11. Comparison of measurement results of the LIDG absorber without and with Fe_3O_4 embedded, (a) TE mode under normal incidence. (b) TE mode under oblique incidence. (c) TM mode under normal incidence. (d) TM mode under oblique incidence.

the increase in the bandwidth of the Fe_3O_4 embedded MMA is mainly owing to the frequency shift to the lower frequency bands, which means that the overall structure had a broader impedance match to free space. This is a significant improvement, as one of the most challenging issues in broadband absorber designs is covering as many lower-frequency bands as possible without compromising the higher-frequency performance and increasing the absorber profile. This improvement is likely to be due to the extra loss provided by Fe_3O_4 .

In the complex permeability, the imaginary part (μ'') represents the loss capability of the magnetic energy. Without Fe_3O_4 , the LIDG is not a ferromagnetic material, and hence, $\mu_r = 1$. When Fe_3O_4 was embedded (even a very small amount), the magnetic loss of the MMA becomes stronger owing to resonance and ohmic loss [45]. It should be noted that the overall concentration of the embedded Fe_3O_4 is crucial because it has an extremely large permeability. An excess percentage of ferro ferric oxide embedding causes a mismatch between the absorber and free space, thus resulting in poor absorption.

Figure 12 presents a comparison of the performances of the two absorbers (with and without embedded Fe_3O_4) in the TE and TM modes. Both the absorbers maintained excellent average absorptivity. The embedded Fe_3O_4 MMA exhibited

a higher average absorption under oblique incidences of TM polarisation. As for the fractional absorption bandwidth, the Fe_3O_4 MMA always has a wider bandwidth.

3.4.3. Comparison of microwave absorption performances. For the purpose of comparison with the previous work, the two main factors of bandwidth and absorber thickness were considered. Pan *et al* reported the application of rGO laminates for ultra-wideband microwave absorption and demonstrated that a coating with a thickness of over 30 mm provided efficient absorption in the range of 2–10.8 GHz, which hindered its conformal and miniature applications [46]. Assal *et al* demonstrated a multiband hybrid layer metamaterial-based array for a microwave absorber, with an absorber thickness of approximately 16.2 mm and a high absorption performance of greater than 95% from 2.6 GHz to 18 GHz [47]. However, its low cutoff frequency of 2.6 GHz did not fully cover the S-band, which is crucial for wireless communication and radar applications. Therefore, for real microwave absorption applications, it is important to reduce the material thickness while maintaining a cutoff frequency that is as low as possible. Our work has presented a significantly improved bandwidth of $>20\%$, especially in the low-frequency region.

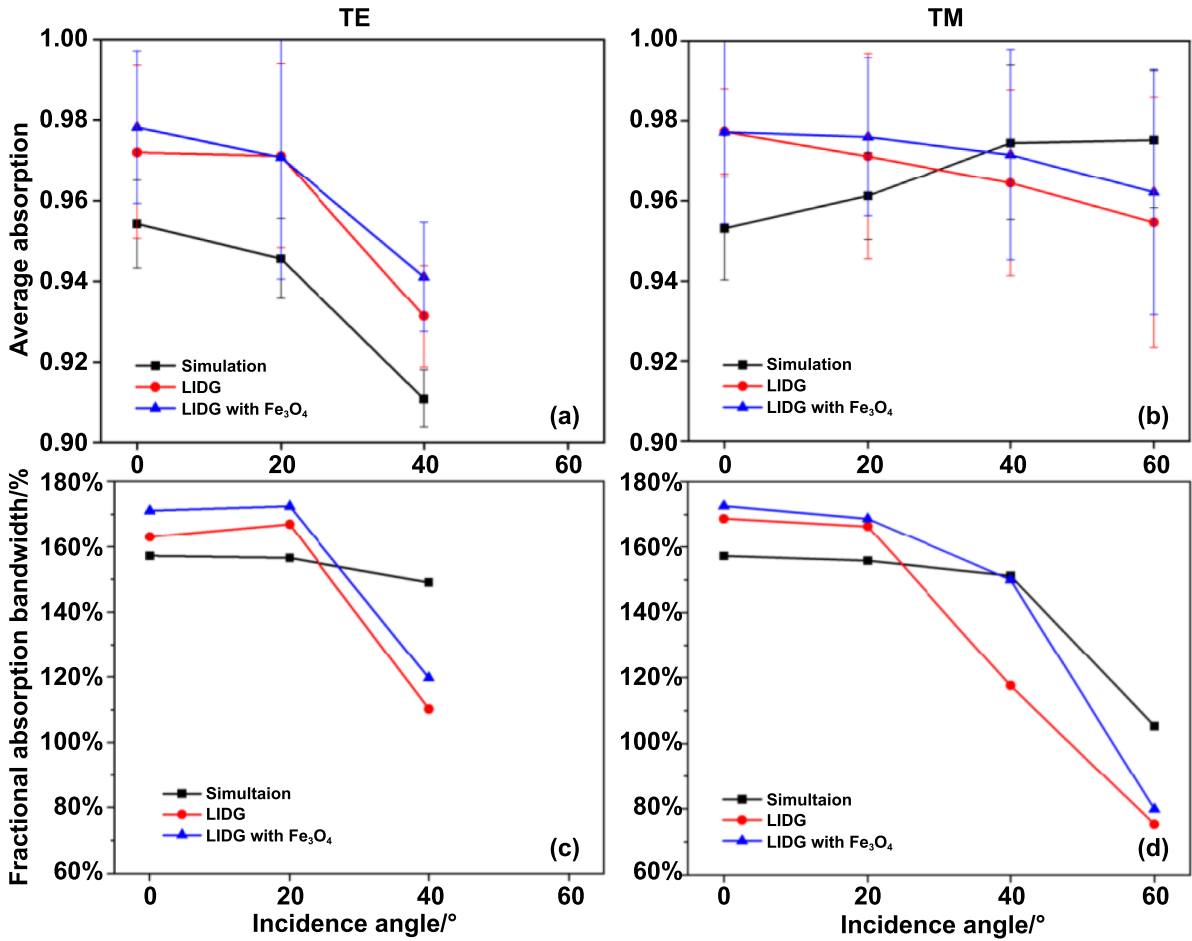


Figure 12. Average absorption and fractional absorption bandwidth comparisons of simulation results, LIDG absorber, and Fe₃O₄ embedded LIDG absorber in the (a,c) TE and (b,d) TM modes.

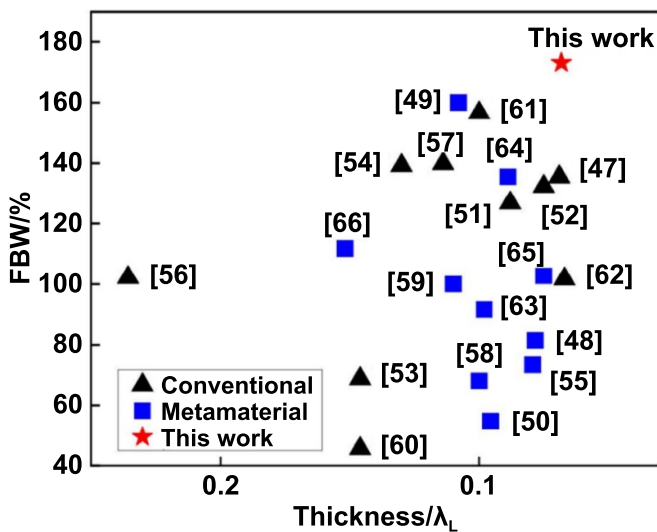


Figure 13. Comparison on fractional bandwidth and relative thickness obtained from absorber studies conducted in recent years.

The absorber, designed and fabricated using LDW, has the widest bandwidth reported thus far, with the lowest thickness in the low-frequency band. Figure 13 presents a comparison of the fractional bandwidth and relative thickness (relative

thickness = thickness/ λ_L , where λ_L is the wavelength corresponding to the minimum operating frequency) of conventional, metamaterial [13, 47–65], and proposed absorbers, thus demonstrating the improvement in the microwave absorption achieved by the metamaterial designed and achieved through LDW.

4. Conclusion

A one-step metamaterial (with negative relative permittivity) synthesis using LDW was demonstrated to produce magnetic Fe₃O₄-nanoparticles-embedded graphene on a flexible PET substrate. The laser-fabricated metamaterial patterns consist of N- and S-doped porous turbostratic graphene with different degrees of crystallisation, which facilitates the precise control of the electrical sheet resistance from 57 to 480 $\Omega \text{ sq}^{-1}$ within a 5% accuracy. The LIDG-based MMA has demonstrated an average absorption coefficient in the range of 97.2%–97.7% for a wide bandwidth of 1.56 GHz–18.3 GHz for microwave incident angles of 0°–40° in both the TE and TM modes. With the addition of magnetic Fe₃O₄ nanoparticles, the bandwidth of the MMA has demonstrated an increase of approximately 4%–8% owing to the extra magnetic loss. The material achieved the highest relative bandwidth and lowest thickness

in the L-to-S band reported till date. This method is simple, allows precise control of the sheet resistance over large areas, and introduces a new avenue for the large-scale manufacturing of metamaterials for microwave absorption applications.

ORCID iD

Yihe Huang  <https://orcid.org/0000-0002-5514-0460>

References

- [1] Landy N I, Sajuyigbe S, Mock J J, Smith D R and Padilla W J 2008 Perfect metamaterial absorber *Phys. Rev. Lett.* **100** 207402
- [2] Xie Y B, Ye S R, Reyes C, Sithikong P, Popa B-I, Wiley B J and Cummer S A 2017 Microwave metamaterials made by fused deposition 3D printing of a highly conductive copper-based filament *Appl. Phys. Lett.* **110** 181903
- [3] Shin Y M, Zhao J F, Baig A, Gamzina D, Barnett L R and Luhmann N C 2010 Micro-fabricable terahertz sheet beam amplifier integrated with broadband metamaterial circuit *Proc. Int. Conf. on Communications and Electronics 2010* (Nha Trang: IEEE) pp 373–8
- [4] Yoo M, Kim H K, Kim S, Tentzeris M and Lim S 2015 Silver nanoparticle-based inkjet-printed metamaterial absorber on flexible paper *IEEE Antennas Wirel. Propag. Lett.* **14** 1718–21
- [5] Momeni-Nasab M, Bidoki S M, Hadizadeh M and Movahhedi M 2020 Ink-jet printed metamaterial microwave absorber using reactive inks *AEU-Int. J. Electron. Commun.* **123** 153259
- [6] Torrisi F et al 2012 Inkjet-printed graphene electronics *ACS Nano* **6** 2992–3006
- [7] Gao Y H, Shi W, Wang W C, Leng Y P and Zhao Y P 2014 Inkjet printing patterns of highly conductive pristine graphene on flexible substrates *Ind. Eng. Chem. Res.* **53** 16777–84
- [8] Ji A, Chen Y M, Wang X Y and Xu C Y 2018 Inkjet printed flexible electronics on paper substrate with reduced graphene oxide/carbon black ink *J. Mater. Sci., Mater. Electron.* **29** 13032–42
- [9] Kao H-L, Cho C-L, Chang L-C, Chen C-B, Chung W-H and Tsai Y-C 2020 A fully inkjet-printed strain sensor based on carbon nanotubes *Coatings* **10** 792
- [10] Tran T S, Dutta N K and Choudhury N R 2018 Graphene inks for printed flexible electronics: graphene dispersions, ink formulations, printing techniques and applications *Adv. Colloid Interface Sci.* **261** 41–61
- [11] Jabari E, Ahmed F, Liravi F, Secor E B, Lin L W and Toyserkani E 2019 2D printing of graphene: a review *2D Mater.* **6** 042004
- [12] Huang X J, Leng T, Georgiou T, Abraham J, Raveendran Nair R, Novoselov K S and Hu Z R 2018 Graphene oxide dielectric permittivity at GHz and its applications for wireless humidity sensing *Sci. Rep.* **8** 43
- [13] Fang Y X, Pan K W, Leng T, Ouslimani H H, Novoselov K S and Hu Z R 2021 Controlling graphene sheet resistance for broadband printable and flexible artificial magnetic conductor-based microwave radar absorber applications *IEEE Trans. Antennas Propag.* **69** 8503–11
- [14] Arapov K, Jaakkola K, Ermolov V, Bex G, Rubingh E, Haque S, Sandberg H, Abbel R, de With G and Friedrich H 2016 Graphene screen-printed radio-frequency identification devices on flexible substrates *Phys. Status Solidi* **10** 812–8
- [15] Pan K W, Fan Y Y, Leng T, Li J S, Xin Z Y, Zhang J W, Hao L, Gallop J, Novoselov K S and Hu Z R 2018 Sustainable production of highly conductive multilayer graphene ink for wireless connectivity and IoT applications *Nat. Commun.* **9** 5197
- [16] Parate K, Pola C C, Rangnekar S V, Mendivelso-Perez D L, Smith E A, Hersam M C, Gomes C L and Claussen J C 2020 Aerosol-jet-printed graphene electrochemical histamine sensors for food safety monitoring *2D Mater.* **7** 034002
- [17] Jia Z R, Lan D, Lin K J, Qin M, Kou K C, Wu G L and Wu H J 2018 Progress in low-frequency microwave absorbing materials *J. Mater. Sci., Mater. Electron.* **29** 17122–36
- [18] Wang B L, Wu Q, Fu Y G and Liu T 2021 A review on carbon/magnetic metal composites for microwave absorption *J. Mater. Sci. Technol.* **86** 91–109
- [19] Koziol P E, Antończak A J, Walczakowski M, Pałka N and Abramski K M 2014. THz structures fabricated in laser direct patterning *Proc. 2014 8th Int. Congress on Advanced Electromagnetic Materials in Microwaves and Optics* (Copenhagen: IEEE) pp 367–9
- [20] Rill M S, Plet C, Thiel M, Staude I, Von Freymann G, Linden S and Wegener M 2008 Photonic metamaterials by direct laser writing and silver chemical vapour deposition *Nat. Mater.* **7** 543–6
- [21] Charipar N A, Charipar K M, Kim H, Kirleis M A, Auyeung R C Y, Smith A T, Mathews S A and Piqué A 2013 Laser processing of 2D and 3D metamaterial structures *Proc. SPIE* **8607** 67–73
- [22] Mathews S A, Mirotznik M, Good B L and Piqué A 2007 Rapid prototyping of frequency selective surfaces by laser direct-write *Proc. SPIE* **6458** 167–80
- [23] Komlenok M S, Lebedev S P, Komandin G A, Piqué A and Konov V I 2018 Fabrication and electrodynamic properties of all-carbon terahertz planar metamaterials by laser direct-write *Laser Phys. Lett.* **15** 036201
- [24] Huang Y H, Zeng L, Liu C G, Zeng D S, Liu Z, Liu X Q, Zhong X L, Guo W and Li L 2018 Laser direct writing of heteroatom (N and S)-doped graphene from a polybenzimidazole ink donor on polyethylene terephthalate polymer and glass substrates *Small* **14** 1803143
- [25] Bai S, Zhou W P, Tao C, Oakes K D and Hu A M 2014 Laser-processed nanostructures of metallic substrates for surface-enhanced Raman spectroscopy *Curr. Nanosci.* **10** 486–96
- [26] Zhou W P, Bridges D, Li R Z, Bai S, Ma Y, Hou T X and Hu A M 2016 Recent progress of laser micro-and nano manufacturing *Sci. Lett. J.* **5** 228
- [27] Zacharatos F, Iliadis N, Kanakis J, Bakopoulos P, Avramopoulos H and Zergioti I 2016 Laser direct writing of 40 GHz RF components on flexible substrates *Opt. Laser Technol.* **79** 108–14
- [28] Peng P, Hu A and Zhou Y 2012 Laser sintering of silver nanoparticle thin films: microstructure and optical properties *Appl. Phys. A* **108** 685–91
- [29] Liu W, Chen Q, Huang Y H, Wang D, Li L and Liu Z 2022 *In situ* laser synthesis of Pt nanoparticles embedded in graphene films for wearable strain sensors with ultra-high sensitivity and stability *Carbon* **190** 245–54
- [30] Sha Y, Peng Y D, Huang K, Li L and Liu Z 2022 3D binder-free integrated electrodes prepared by phase separation and laser induction (PSLI) method for oxygen electrocatalysis and zinc-air battery *Adv. Energy Mater.* **12** 2200906
- [31] Ehrensberger K, Schmalte H W, Oswald H R and Reller A 1999 Thermochemical reactivity of transition metal acetates and of a novel DMSO solvate of iron(II) acetate in molecular hydrogen *J. Therm. Anal. Calorim.* **57** 139–49
- [32] Normikman H, Malek M F B A, Ahmed M, Wee F H, Soh P J, Al-Hadi A A, Ghani S A, Hasnain A and Taib M N 2011

- Setup and results of pyramidal microwave absorbers using rice husks *Prog. Electromagn. Res.* **111** 141–61
- [33] Magill E and Wheeler H 1966 Wide-angle impedance matching of a planar array antenna by a dielectric sheet *IEEE Trans. Antennas Propag.* **14** 49–53
- [34] Paparazzo E 1987 XPS and auger spectroscopy studies on mixtures of the oxides SiO₂, Al₂O₃, Fe₂O₃ and Cr₂O₃ *J. Electron Spectrosc. Relat. Phenom.* **43** 97–112
- [35] Dey A, Zubko M, Kusz J, Reddy V R and Bhattacharjee A 2020 Effect of reaction protocol on the nature and size of iron oxide nano particles obtained through solventless synthesis using iron(II)acetate: structural, magnetic and morphological studies *SN Appl. Sci.* **2** 193
- [36] Huang Y H, Sepioni M, Whitehead D, Liu Z, Guo W, Zhong X L, Gu H and Li L 2020 Rapid growth of large area graphene on glass from olive oil by laser irradiation *Nanotechnology* **31** 245601
- [37] Lin Z, Ye X H, Han J P, Chen Q, Fan P X, Zhang H J, Xie D, Zhu H W and Zhong M L 2015 Precise control of the number of layers of graphene by picosecond laser thinning *Sci. Rep.* **5** 11662
- [38] Chae S et al 2020 Anomalous restoration of sp² hybridization in graphene functionalization *Nanoscale* **12** 13351–9
- [39] Dean C R et al 2010 Boron nitride substrates for high-quality graphene electronics *Nat. Nanotechnol.* **5** 722–6
- [40] Mir S H, Yadav V K and Singh J K 2020 Recent advances in the carrier mobility of two-dimensional materials: a theoretical perspective *ACS Omega* **5** 14203–11
- [41] Tian Z S, Li J T, Zhu G Y, Lu J F, Wang Y Y, Shi Z L and Xu C X 2016 Facile synthesis of highly conductive sulfur-doped reduced graphene oxide sheets *Phys. Chem. Chem. Phys.* **18** 1125–30
- [42] Griffiths D J 2005 *Introduction to Electrodynamics* (Trenton, NJ: American Association of Physics Teachers)
- [43] Fang Y X and Hu Z R 2020 Ultra-wideband polarization-insensitive thin microwave absorber composed of triple-layer resistive surfaces *Proc. 2020 14th European Conf. on Antennas and Propagation* (Copenhagen: IEEE) pp 1–4
- [44] Bhattacharyya S, Ghosh S and Srivastava K V 2014 Equivalent circuit model of an ultra-thin polarization-independent triple band metamaterial absorber *AIP Adv.* **4** 097127
- [45] Wang L N, Jia X L, Li Y F, Yang F, Zhang L Q, Liu L P, Ren X and Yang H T 2014 Synthesis and microwave absorption property of flexible magnetic film based on graphene oxide/carbon nanotubes and Fe₃O₄ nanoparticles *J. Mater. Chem. A* **2** 14940–6
- [46] Pan K W, Leng T, Song J, Ji C Y, Zhang J W, Li J S, Novoselov K S and Hu Z R 2020 Controlled reduction of graphene oxide laminate and its applications for ultra-wideband microwave absorption *Carbon* **160** 307–16
- [47] El Assal A, Breiss H, Benzerga R, Sharaiha A, Jrad A and Harmouch A 2020 Toward an ultra-wideband hybrid metamaterial based microwave absorber *Micromachines* **11** 930
- [48] Cao Z, Yao G J, Zha D C, Zhao Y, Wu Y, Miao L, Bie S W and Jiang J J 2022 Impedance well effect from circuit analysis and new design concepts for ultrabroadband passive absorber *IEEE Trans. Antennas Propag.* **70** 9942–6
- [49] de Araújo J B O, Siqueira G L, Kemptner E, Weber M, Junqueira C and Mosso M M 2020 An ultrathin and ultrawideband metamaterial absorber and an equivalent-circuit parameter retrieval method *IEEE Trans. Antennas Propag.* **68** 3739–46
- [50] Kundu D, Mohan A and Chakrabarty A 2016 Single-layer wideband microwave absorber using array of crossed dipoles *IEEE Antennas Wirel. Propag. Lett.* **15** 1589–92
- [51] Shang Y P, Shen Z X and Xiao S Q 2013 On the design of single-layer circuit analog absorber using double-square-loop array *IEEE Trans. Antennas Propag.* **61** 6022–9
- [52] Li S J, Gao J, Cao X Y, Li W Q, Zhang Z and Zhang D 2014 Wideband, thin, and polarization-insensitive perfect absorber based the double octagonal rings metamaterials and lumped resistances *J. Appl. Phys.* **116** 043710
- [53] Olszewska-Placha M, Salski B, Janczak D, Bajurko P R, Gwarek W and Jakubowska M 2015 A broadband absorber with a resistive pattern made of ink with graphene nano-platelets *IEEE Trans. Antennas Propag.* **63** 565–72
- [54] Wei J F et al 2019 Flexible design and realization of wideband microwave absorber with double-layered resistor loaded FSS *J. Phys. D: Appl. Phys.* **52** 185101
- [55] Shen Z Y, Huang X J, Yang H L, Xiang T Y, Wang C W, Yu Z T and Wu J 2018 An ultra-wideband, polarization insensitive, and wide incident angle absorber based on an irregular metamaterial structure with layers of water *J. Appl. Phys.* **123** 225106
- [56] Huang X J, Hu Z R and Liu P G 2014 Graphene based tunable fractal Hilbert curve array broadband radar absorbing screen for radar cross section reduction *AIP Adv.* **4** 117103
- [57] He Z D, Wu L W, Liu Y, Lu Y, Wang F Q, Shao W, Fu S H and Tong G X 2020 Ultrawide bandwidth and large-angle electromagnetic wave absorption based on triple-nested helix metamaterial absorbers *J. Appl. Phys.* **127** 174901
- [58] Yoo M and Lim S 2014 Polarization-independent and ultrawideband metamaterial absorber using a hexagonal artificial impedance surface and a resistor-capacitor layer *IEEE Trans. Antennas Propag.* **62** 2652–8
- [59] Cao Z W, Li H R, Wu Y, Yao G J, Zhao Y, Huang Z, Guo S, Miao L and Jiang J J 2022 Backend-balanced-impedance concept for reverse design of ultra-wideband absorber *IEEE Trans. Antennas Propag.* **70** 11217–22
- [60] Luo G Q, Yu W L, Yu Y F, Zhang X H and Shen Z X 2020 A three-dimensional design of ultra-wideband microwave absorbers *IEEE Trans. Microw Theory Tech.* **68** 4206–15
- [61] Sambhav S, Ghosh J and Singh A K 2021 Ultra-wideband polarization insensitive thin absorber based on resistive concentric circular rings *IEEE Trans. Electromagn. Compat.* **63** 1333–40
- [62] Kalraiya S, Chaudhary R K and Abdalla M A 2019 Design and analysis of polarization independent conformal wideband metamaterial absorber using resistor loaded sector shaped resonators *J. Appl. Phys.* **125** 134904
- [63] Zhao Y F, Li S Y, Jiang Y Y, Gu C Q, Liu L L and Li Z 2021 An ultra-wideband and wide-angle optically transparent flexible microwave metamaterial absorber *J. Appl. Phys.* **54** 275101
- [64] Zheng Y L, Chen K, Jiang T, Zhao J M and Feng Y J 2019 Multi-octave microwave absorption via conformal metamaterial absorber with optical transparency *J. Phys. D: Appl. Phys.* **52** 335101
- [65] Yao Z X, Xiao S Q, Jiang Z G, Yan L and Wang B-Z 2020 On the design of ultrawideband circuit analog absorber based on quasi-single-layer FSS *IEEE Antennas Wirel. Propag. Lett.* **19** 591–5